



B and Fe co-doped Co₂P hollow nanocubes for nitrate electroreduction to ammonia

Jing Miao^a, Qingling Hong^b, Liping Liang^a, Guomin Li^a, Zhihong Liu^{c,*}, Shibin Yin^{d,*}, Yu Chen^{b,*}

^a School of Materials Science and Engineering, Taiyuan University of Science and Technology, Taiyuan 030024, China

^b School of Materials Science and Engineering, Shaanxi Normal University, Xi'an 710062, China

^c School of Chemistry and Chemical Engineering, Shaanxi Normal University, Xi'an 710062, China

^d Guangxi Key Laboratory of Electrochemical Energy Materials, School of Chemistry and Chemical Engineering, Guangxi University, Nanning 530004, China

ARTICLE INFO

Article history:

Received 8 June 2023

Revised 12 August 2023

Accepted 15 August 2023

Available online 17 August 2023

Keywords:

Nitrate electroreduction reaction

Ammonia synthesis

Transition metal phosphides

Hollow nanocubes

ABSTRACT

Nitrate (NO₃⁻) electroreduction reaction (NO₃⁻-RR) provides an attractive and sustainable route for NO₃⁻ pollution mitigation or energy-saved ammonia (NH₃) synthesis. In this work, high-quality B and Fe co-doped Co₂P hollow nanocubes (B/Fe-Co₂P HNCs) are successfully synthesized through simultaneous boronation-phosphorization treatment, which reveal outstanding selectivity, activity, stability for the NO₃⁻ to NH₃ conversion in neutral electrolyte because of big surface area, fast mass transport, super-hydrophilic surface, and optimized electronic structure. B/Fe-Co₂P HNCs can achieve the high NH₃ yield rate (22.67 mg h⁻¹ mg_{cat}⁻¹) as well as Faradaic efficiency (97.54%) for NO₃⁻-RR, greatly outperforming most of non-precious metal based NO₃⁻-RR electrocatalysts.

© 2023 Published by Elsevier B.V. on behalf of Chinese Chemical Society and Institute of Materia Medica, Chinese Academy of Medical Sciences.

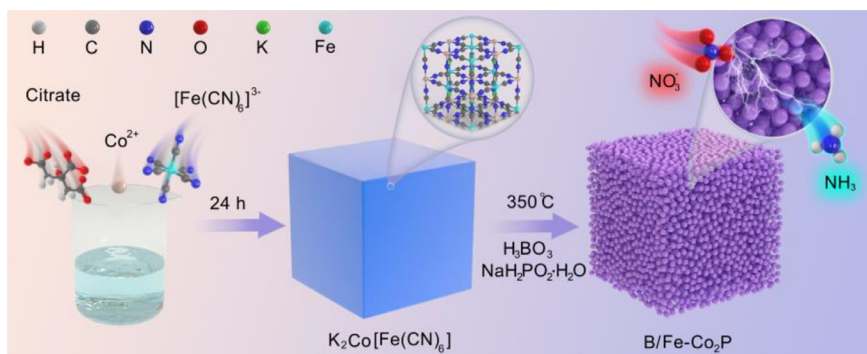
Ammonia (NH₃) not only acts as a critical industrial raw chemical in the agriculture, textile, pharmaceutical and plastic industries, but also serves as an emissions-less and efficient energy carrier [1,2]. Compared with the traditional Haber-Bosch process at high pressures and high temperatures, the electrochemical synthesis method can provide an environmentally friendly and energy-efficient approach for large-scale NH₃ production [3]. At present, nitrogen electroreduction reaction suffers from the highly stable N≡N triple bond (ca. 941 kJ/mol) as well as unsatisfactory Faradaic efficiency [4]. In contrast, the nitrate (NO₃⁻) electroreduction reaction (NO₃⁻-RR) is considered as an attractive electrochemical method for NH₃ production because of the high solubility of NO₃⁻ in water and the small dissociation energy of N=O double bond (ca. 204 kJ/mol) [5–7]. In fact, NO₃⁻ pollution in drinking water causes severe problems to human health, which mainly originates from the excessive use of nitrogen-containing fertilizer and the improper discharge of wastewater [8,9]. From the energy-saving and environmental protection perspectives, thus, NO₃⁻-RR is highly attractive to harness NO₃⁻ contamination to produce valuable NH₃. However, the competing hydrogen evolution reaction (HER) and

complex eight-electron transfer process may lead to the low NH₃ yield and selectivity [10,11].

Recently, transition metal phosphides (TMPs) are attractive electrocatalysts because of their low-cost, impressive activity and positive reduction potential for NO₃⁻-RR [12–14]. To achieve high activity, selectivity, and durability of TMPs electrocatalysts for NO₃⁻-RR, many efforts have been devoted to exquisitely control their morphology, optimize their chemical composition, and modify their electronic structure [15,16]. For example, Li and co-workers successfully synthesized Fe-doped CoP nanohoops, which revealed improved NO₃⁻-RR activity compared to CoP nanohoops due to electronic regulation function of Fe atoms [17]. Among various nanostructures with different morphologies, hollow nanostructures can offer great benefits for boosting their electrocatalytic performance, which efficiently provide more exposed active sites and shorten the charge transport pathways [18–21]. In addition, boron (B) doping is an efficient approach to boost the intrinsic activity of transition element-based nanostructures for various electrocatalytic reactions, such as B-doped Fe₇S₈/FeS₂ electrocatalysts for alkaline HER [22], B doped cobalt oxide nanocrystals for oxygen evolution reaction [23], and B, P co-doped Pd nanothorn arrays for NO₃⁻-RR [24]. Mainly, B atoms can well rearrange the inhomogeneous spin and charge density of metal atoms, originating from the easy coordination with metal atoms [25]. Inspired by this, it is

* Corresponding authors.

E-mail addresses: liuzh@snnu.edu.cn (Z. Liu), yinshibin@gxu.edu.cn (S. Yin), ndchenyu@gmail.com (Y. Chen).



Scheme 1. The synthetic strategy of B/Fe-Co₂P HNCs.

highly desired to synthesize B-doped porous TMPs nanostructures for the NO₃[−]RR.

In this work, we successfully synthesized B and Fe co-doped Co₂P hollow nanocubes (B/Fe-Co₂P HNCs) and further investigated the NO₃[−]RR performance. The introduction of electron-deficient B atoms could efficiently rearrange the electronic structure of Fe-Co₂P HNCs. Besides, the hollow and porous architecture could provide high surface area, abundant active sites and available mass transfer pathways. Benefiting from the hollow nanostructures, well-defined void space, and tunable chemical compositions, B/Fe-Co₂P HNCs exhibited an outstanding selectivity, activity, stability for the NO₃[−] to NH₃ conversion in neutral Na₂SO₄ electrolyte. B/Fe-Co₂P HNCs with long-term stability and high activity provide a facile strategy for synthesis NH₃ and elimination of NO₃[−] contamination.

B/Fe-Co₂P HNCs were synthesized through successive precipitation transformation and boronation-phosphidation methods, as illustrated in Scheme 1. Prussian blue analogues (PBAs) are recognized as popular precursor for TMPs synthesis because of their tunable chemical composition, large specific surface areas, and high porosity [26].

First, CoFe-PBA HNCs were easily synthesized through coprecipitation method (see experimental section in Supporting information for the detail). Both the scanning electron microscopy (SEM) and transmission electron microscopy (TEM) characterization show that CoFe-PBA HNCs have a well-defined cubic morphology, uniform size (ca. 300–400 nm) and smooth surface (Fig. S1 in Supporting information). In X-ray diffraction (XRD) characterization, all diffraction peaks are well indexed to K₂CoFe(CN)₆ crystal (JCPDS No. 75-0038) (Fig. S2 in Supporting information). Thus, SEM and XRD characterization confirm the successful synthesis of CoFe-PBA HNCs. After simultaneous boronation-phosphorization process, the energy dispersive X-ray (EDX) characterization displays the co-existence of B, Fe, Co and P elements whereas K and N elements of PBA are not observed (Fig. 1a). The XRD pattern of as-prepared sample matches well with Co₂P crystal (JCPDS No. 32-0306) and the characteristic peak of PBA precursor disappear completely (Fig. 1b). Thus, we can be concluded that PBA is completely converted into B/Fe-Co₂P HNCs. For comparison, Fe-Co₂P HNCs without B-doping were synthesized by phosphorization treatment (Fig. S3 in Supporting information). Compared with Fe-Co₂P HNCs, the main diffraction peaks of B/Fe-Co₂P HNCs shift positively, which can be attributed to B doping [27,28]. According to nitrogen adsorption-desorption test, the surface area of B/Fe-Co₂P HNCs is 42.4 m²/g (Fig. 1c), suggesting that the hollow porous B/Fe-Co₂P HNCs can offer ample accessible active sites. Meanwhile, B/Fe-Co₂P HNCs show a smaller contact angle compared to Fe-Co₂P HNCs (Fig. 1d), indicating that the introduction of B atoms can provide superhydrophilic surface. The superhydrophilic surface can facilitate electrolyte adsorption and electron transfer processes [24].

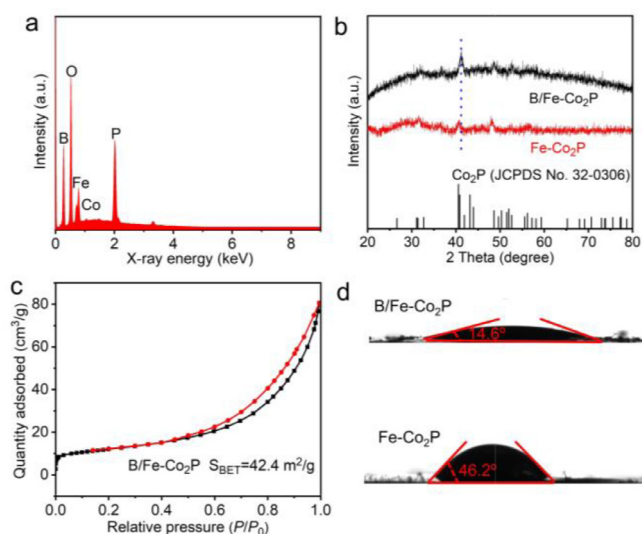


Fig. 1. (a) EDX spectrum, (b) XRD pattern, and (c) nitrogen adsorption-desorption isotherm of B/Fe-Co₂P HNCs, (d) the contact angle of B/Fe-Co₂P HNCs and Fe-Co₂P HNCs.

The hard template strategy can generally preserve the initial morphology of precursor. During the boronation-phosphorization process, CoFe-PBA HNCs are easily decomposed into lesser broken cubes with the rough and porous feature, indicating that CoFe-PBA HNCs are successfully converted into B/Fe-Co₂P HNCs (Figs. 2a and b). By adjusting the mass ratio of B and P, B/Fe-Co₂P HNCs with different B/P mass ratio can also be obtained (Fig. S4 in Supporting information). TEM image clearly reveals the regular and large interior spaces within ultrafine nanoparticles embedded in the outer face (Fig. 2c). High-resolution TEM image distinctly reveals the lattice fringes of 0.175 and 0.221 nm (Fig. 2d), corresponding to (020) and (112) planes of Co₂P [29,30]. Elemental mapping characterization shows that Co, P, B, and Fe elements are homogeneously distributed on the nanocubes (Fig. 2e), confirming the B and Fe co-doping, again.

The surface component and valence state of B/Fe-Co₂P HNCs were examined by X-ray photoelectron spectroscopy (XPS). In the Co 2p spectrum (Fig. 3a), the peaks at 795.5 and 780.1 eV correspond to 2p_{1/2} and 2p_{3/2} orbits of Co²⁺ species, and the peaks at 797.2 and 782.1 eV are attributed to 2p_{1/2} and 2p_{3/2} orbits of Co³⁺ species. The two broad peaks at 785.6 and 802.5 eV are assigned to the satellite peaks [31,32]. In the Fe 2p spectrum (Fig. 3b), two peaks at 724.5 and 710.7 eV can be ascribed to 2p_{1/2} and 2p_{3/2} orbits of Fe²⁺ species, whereas the peaks at 727.6 and 713.3 eV correspond to 2p_{1/2} and 2p_{3/2} orbits of Fe³⁺ species, along with two shakeup satellite peaks at 717.7 and 733.3 eV [33,34]. Particularly,

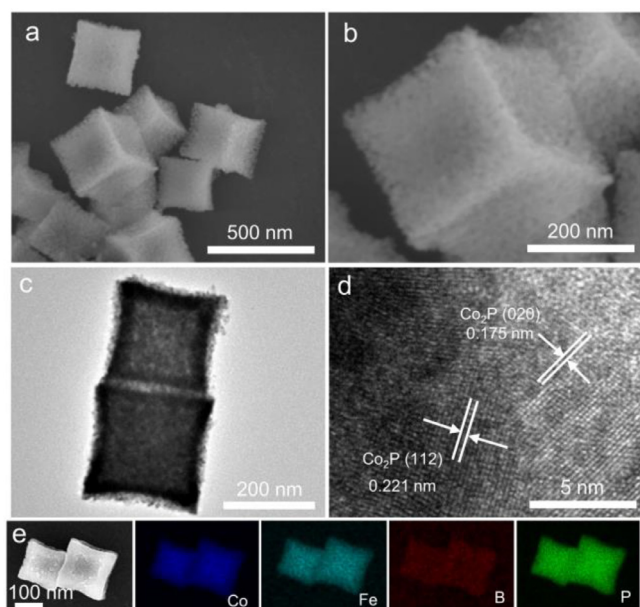


Fig. 2. (a, b) SEM images, (c) TEM image, (d) high-resolution TEM image, and (e) EDX elemental mapping images of B/Fe-Co₂P HNCs.

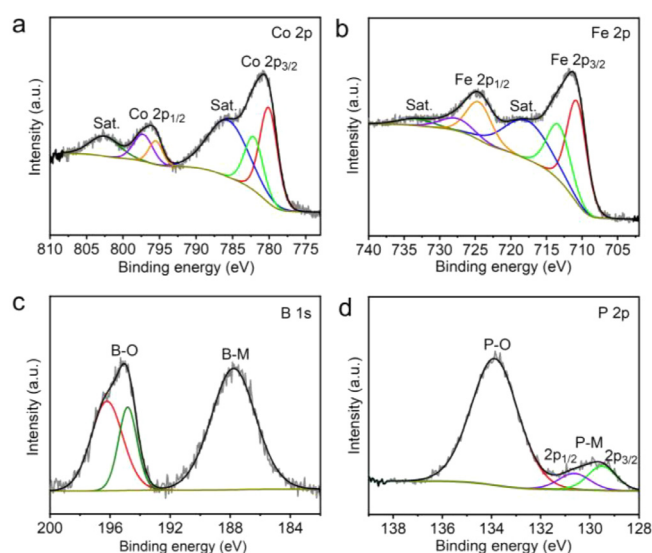


Fig. 3. (a) Co 2p, (b) Fe 2p, (c) B 1s, and (d) P 2p XPS spectra of B/Fe-Co₂P HNCs.

the binding energies of Co 2p and Fe 2p negatively shift after B doping (Fig. S5 in Supporting information), suggesting the electron interaction between metal atom and B atom because of the electron-deficient nature of B [35,36]. In the B 1s spectrum (Fig. 3c), the peak at 187.8 eV correspond to the peak of metallic B [37]. The peaks at higher binding energy (194.8 eV, 196.2 eV) correspond to the oxidic boron species [38,39]. In the P 2p spectrum (Fig. 3d), the huge peak of 133.9 eV belongs to P-O, and the two peaks at 129.3 and 130.4 eV can be ascribed to TMPs, which is constant with reported TMPs nanostructures [40,41].

The NO₃⁻RR performance of B/Fe-Co₂P HNCs and Fe-Co₂P HNCs were investigated in 0.5 mol/L Na₂SO₄ electrolyte with and without 50 mmol/L NaNO₃. Both Fe-Co₂P HNCs and B/Fe-Co₂P HNCs display an obvious electroactivity for NO₃⁻RR, reflecting the cathodic current markedly increases after the addition of NO₃⁻ into 0.5 mol/L Na₂SO₄ electrolyte. Compared with Fe-Co₂P HNCs with-

out B doping, B/Fe-Co₂P HNCs exhibit a more positive onset potential and a bigger reduction peak current density for NO₃⁻RR, implying the outstanding NO₃⁻RR catalytic activity (Fig. 4a). This phenomenon further suggests that the intrinsic NO₃⁻RR activity of Fe-Co₂P HNCs is significantly enhanced after B doping. Since XPS measurements show the introduction of B atoms can efficiently regulate the electronic structure of Fe-Co₂P HNCs, the electronic effect is responsible for intrinsic activity enhancement of Fe-Co₂P HNCs due to B doping. Among B/Fe-Co₂P HNCs with different B/P ratio, B/Fe-Co₂P HNCs (B:P = 2:1) has the highest NO₃⁻RR (Fig. S6 in Supporting information), which in turn confirms that both B and P atoms have obvious influence on NO₃⁻RR activity enhancement. To study the activity and selectivity of B/Fe-Co₂P HNCs for NO₃⁻RR, the reactant and reductive products were determined by the chronoamperometry tests at various applied potentials. After chronoamperometry tests for 3 h, colorimetric methods were used to quantify the NH₃ yields and Faradaic efficiency (Figs. S7 and S8 in Supporting information). Upon varying the applied potential from -0.5 V to -0.9 V (vs. RHE), the NH₃ production rate and conversion rate of NO₃⁻RR at B/Fe-Co₂P HNCs gradually increase, while the Faradaic efficiency of NH₃ at B/Fe-Co₂P HNCs displays a volcanic shape (Fig. 4b), similar to Fe-Co₂P HNCs (Fig. S9 in Supporting information). Compared with Fe-Co₂P HNCs, B/Fe-Co₂P HNCs displays larger NH₃ production rate and Faradaic efficiency under same potential. For example, B/Fe-Co₂P HNCs can achieve the NH₃ yield of 22.67 mg h⁻¹ mg_{cat}⁻¹ and the Faradaic efficiency of 97.54% at -0.70 V potential (Fig. 4c), much higher than that of Fe-Co₂P HNCs, suggesting high activity and selectivity of B/Fe-Co₂P HNCs for the NO₃⁻ to NH₃ conversion. The control experiment performed in 0.5 mol/L Na₂SO₄ electrolyte only generates negligible NH₃, excluding the interference of catalysts and environmental contaminants (Fig. S10 in Supporting information). Impressively, B/Fe-Co₂P HNCs have higher NH₃ yield and Faradaic efficiency than most previously reported non-precious metal electrocatalysts for NO₃⁻RR (Table S1 in Supporting information), further demonstrating the high electroactivity of B/Fe-Co₂P HNCs. Electrochemical impedance spectroscopy (EIS) characterization displays that the charge transfer resistance of NO₃⁻RR at B/Fe-Co₂P HNCs (49.3 Ω) is much smaller than that at Fe-Co₂P HNCs (125 Ω), suggesting that the B doping accelerates the reaction kinetics of NO₃⁻RR (Fig. 4d) [24].

Benefiting from the small particle size and porous structure, B/Fe-Co₂P HNCs can provide a high surface area and expose affluent active sites, facilitating the NO₃⁻ to NH₃ conversion [42,43]. The electrochemical double-layer capacitances (*C*_{dl}) are estimated via cycling voltammetry (CV) curves under different scan rates (Fig. S11 in Supporting information). The *C*_{dl} value (22.41 mF/cm²) of B/Fe-Co₂P HNCs is close to that of Fe-Co₂P HNCs (21.87 mF/cm²), indicating that the electrochemical active surface area of B/Fe-Co₂P HNCs is close to that of Fe-Co₂P HNCs. Thus, the area effect is not a main factor for activity enhancement of B/Fe-Co₂P HNCs. In fact, the doped B atoms can act as Lewis acid active sites to better adsorb NO₃⁻, which accelerates the electroreduction of NO₃⁻ to NH₃ [23,44]. Meanwhile, B/Fe-Co₂P HNCs show a smaller contact angle compared to Fe-Co₂P HNCs, indicating that the introduction of B atoms can provide superhydrophilic surface [45]. Additionally, B doping can effectively optimize the charge density and redistribute the inhomogeneous spin, which is favorable for adsorption kinetics and reduce the reaction energy barrier during NO₃⁻RR [46,47]. As a result, B/Fe-Co₂P exhibits extremely outstanding NO₃⁻RR electroactivity.

Furthermore, the durability of B/Fe-Co₂P HNCs was investigated by chronoamperometry test. Chronoamperometric curve reveals that B/Fe-Co₂P HNCs can be sustained for 30 h with negligible decay during NO₃⁻RR, revealing the excellent stability and practical application for electrochemical NH₃ production (Fig. 5a). Af-

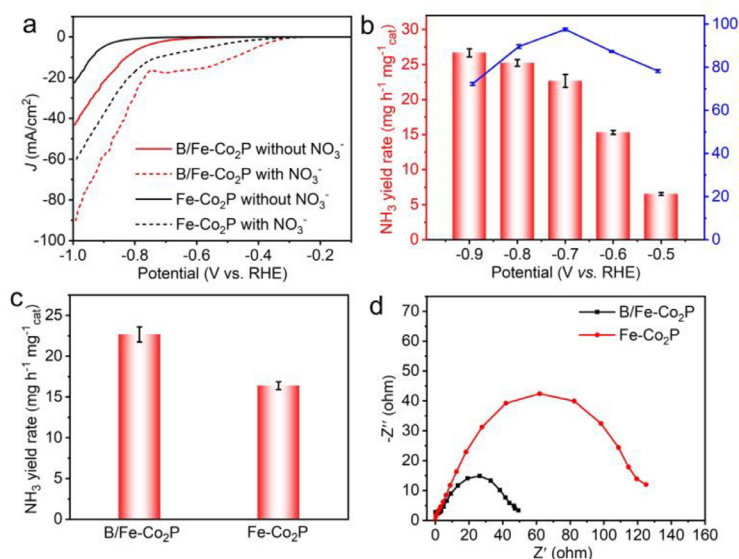


Fig. 4. (a) LSV curves of B/Fe-Co₂P HNCs and Fe-Co₂P HNCs in 0.5 mol/L Na₂SO₄ with and without 50 mmol/L NaNO₃ at 5 mV/s. (b) Faradaic efficiency and NH₃ yield rate of NO₃⁻RR at B/Fe-Co₂P HNCs at different potentials. (c) the NH₃ yield rates of NO₃⁻RR at B/Fe-Co₂P HNCs and Fe-Co₂P HNCs. (d) Nyquist plots of B/Fe-Co₂P HNCs and Fe-Co₂P HNCs.

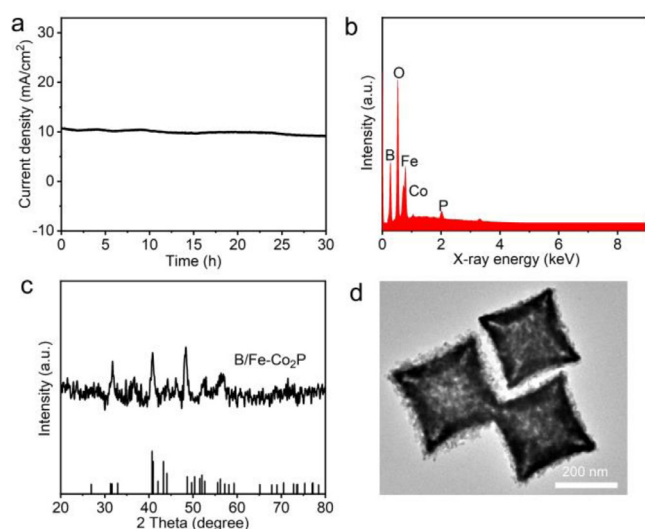


Fig. 5. (a) Chronoamperometric curve of B/Fe-Co₂P HNCs in 0.5 mol/L Na₂SO₄ + 0.05 mol/L NaNO₃ electrolyte at -0.70 V potential. (b) EDX spectrum, (c) XRD pattern, and (d) TEM image of B/Fe-Co₂P HNCs after chronoamperometry test.

ter long-time electrolysis, EDX, XRD and TEM characterizations display that chemical composition, morphology and structure remain nearly unchanged, revealing stability of B/Fe-Co₂P toward NO₃⁻RR (Figs. 5b-d).

In summary, we have rationally designed and synthesized B/Fe-Co₂P HNCs with an open structure and unique hollow interior. Thanks to superhydrophilic surface and abundant active sites, the obtained B/Fe-Co₂P HNCs show excellent electrocatalytic activity for NO₃⁻ to NH₃ conversion. B/Fe-Co₂P HNCs show an impressive NH₃ production rate of 22.67 mg h⁻¹ mg_{cat}⁻¹ and Faradaic efficiency of 97.54%, much superior to the most reported non-precious metal NO₃⁻RR electrocatalysts in neutral media. This work not only highlights a new boronation-phosphorization way for the nanomaterials synthesis but also points out the high-performance of B/Fe-Co₂P HNCs for NO₃⁻ removal and NH₃ synthesis.

Declaration of competing interest

The authors declare that they have no known competing financial interests or personal relationships that could have appeared to influence the work reported in this paper.

Acknowledgments

This work is supported by Natural Science Foundation of Shanxi Province (No. 202203021222213), Taiyuan University of Science and Technology Scientific Research Initial Funding (No. 20222091), National Natural Science Foundation of China (No. 22073061), Science and Technology Innovation Team of Shaanxi Province (No. 2023-CX-TD-27), Fundamental Research Funds for the Central Universities (No. GK202202001).

Supplementary materials

Supplementary material associated with this article can be found, in the online version, at doi:10.1016/j.ccllet.2023.108935.

References

- [1] D.F. Qi, F. Lv, T.R. Wei, et al., *Nano Res. Energy* 1 (2022) e9120022.
- [2] Z.B. Yao, S.Q. Liu, H.H. Liu, et al., *Adv. Funct. Mater.* 33 (2022) 2209843.
- [3] J. Liang, Q. Liu, A.A. Alshehri, et al., *Nano Res. Energy* 1 (2022) e9120010.
- [4] Y.M. Huang, J. Long, Y.T. Wang, et al., *ACS Appl. Mater. Interfaces* 13 (2021) 54967–54973.
- [5] Z.X. Ge, T.J. Wang, Y. Ding, et al., *Adv. Energy Mater.* 12 (2022) 2103916.
- [6] Y. Xu, M.Z. Wang, K.L. Ren, et al., *J. Mater. Chem. A* 9 (2021) 16411–16417.
- [7] Q.L. Hong, B.Q. Miao, T.J. Wang, et al., *Energy Lab* 1 (2023) 220022.
- [8] Y.T. Wang, W. Zhou, R.R. Jia, et al., *Angew. Chem. Int. Ed.* 59 (2020) 5350–5354.
- [9] Q. Li, Y.N. Liu, Z. Wan, et al., *Chin. Chem. Lett.* 33 (2022) 3835–3841.
- [10] Q.F. Yao, J.B. Chen, S.Z. Xiao, et al., *ACS Appl. Mater. Interfaces* 13 (2021) 30458–30467.
- [11] J.M. Cai, Y.Y. Wei, A. Cao, et al., *Appl. Catal. B: Environ.* 316 (2022) 121683.
- [12] G.L. Wen, J. Liang, Q. Liu, et al., *Nano Res.* 15 (2022) 9972–9977.
- [13] Q.L. Hong, J. Zhou, Q.G. Zhai, et al., *Chem. Commun.* 57 (2021) 11621–11624.
- [14] C.M. Li, D.Q. Zhu, S.S. Cheng, et al., *Chin. Chem. Lett.* 33 (2022) 1141–1153.
- [15] S.H. Ye, Z.D. Chen, G.K. Zhang, et al., *Energy Environ. Sci.* 15 (2022) 760.
- [16] S.L. Chen, H. Jang, J. Wang, et al., *J. Mater. Chem. A* 8 (2020) 2099.
- [17] Q.L. Hong, Z.N. Zhang, X.H. Wang, et al., *Inorg. Chem.* 61 (2022) 4397–14402.
- [18] N.Y. Wei, M.Y. Mao, J. Wu, et al., *Fuel* 319 (2022) 123637.
- [19] M.X. Chen, F.T. Kong, H.L. Yao, et al., *Chem. Eng. J.* 45 (2023) 139820.
- [20] Y. Wang, Y.Z. Wang, H.W. Gao, et al., *Chem. Eng. J.* 451 (2023) 138515.

- [21] Y.L. Yang, Y.R. Wang, G.K. Gao, et al., *Chin. Chem. Lett.* 33 (2022) 1439–1444.
- [22] J. Wu, Q. Zhang, K. Shen, et al., *Adv. Funct. Mater.* 32 (2022) 2107802.
- [23] M.Q. Yu, C. Weidenthaler, Y. Wang, et al., *Angew. Chem. Int. Ed.* 61 (2022) e202211543.
- [24] Y. Xu, Y.W. Sheng, M.Z. Wang, et al., *J. Mater. Chem. A* 1 (2022) 16290.
- [25] K. Deng, W.X. Wang, Q.Q. Mao, et al., *Small* 18 (2022) 2203020.
- [26] G.X. Zhang, Y.L. Li, X. Xiao, et al., *Nano Lett.* 21 (2021) 3016–3025.
- [27] S.H. Wang, P. Wang, X.F. Sun, et al., *Appl. Catal. B: Environ.* 297 (2021) 120386.
- [28] Y. Lin, K. Sun, X.M. Chen, et al., *J. Energy Chem.* 55 (2021) 92–101.
- [29] Y. Xu, J. Mo, J.F. Long, et al., *J. Energy Chem.* 73 (2022) 322–329.
- [30] X.J. Zhao, T.Q. Gao, W.H. Ren, et al., *J. Energy Chem.* 75 (2022) 250–259.
- [31] Q. Liu, L.S. Xie, J. Liang, et al., *Small* 18 (2022) 2106961.
- [32] Y. Jia, Y.G. Ji, Q. Xue, et al., *ACS Appl. Mater. Interfaces* 13 (2021) 45521–45527.
- [33] J. Miao, X.J. Zhao, H.Y. Hu, et al., *ACS Appl. Nano Mater.* 5 (2022) 4948–4957.
- [34] Q.M. Chen, Q.C. Zhang, H.B. Liu, et al., *Small* 17 (2021) 2007858.
- [35] F.L. Gou, H. Wang, M.M. Fu, et al., *Appl. Surf. Sci.* 612 (2023) 155872.
- [36] Y.H. Li, H.J. Yu, Z.Q. Wang, et al., *Chem. Commun.* 55 (2019) 14745–14748.
- [37] Z.Q. Wang, M. Li, P. Wang, et al., *Chem. Eng. J.* 449 (2022) 137771.
- [38] F.G. Wang, B. Liu, H.Y. Wang, et al., *J. Colloid Interface Sci.* 610 (2022) 173–181.
- [39] W.J. Jiang, S. Niu, T. Tang, et al., *Angew. Chem. Int. Ed.* 56 (2017) 1–7.
- [40] G. Ma, N. Yang, Y.F. Xue, et al., *ACS Appl. Mater. Interfaces* 13 (2021) 42763–42772.
- [41] J. Wang, H. Cheng, S.Y. Ren, et al., *J. Mater. Chem. A* 8 (2020) 16018–16023.
- [42] X.Y. Zhang, G. Ma, L.L. Shui, et al., *Chem. Eng. J.* 430 (2022) 132666.
- [43] H.Y. Zhou, B.Y. Xiong, L.S. Chen, et al., *J. Mater. Chem. A* 8 (2020) 20286.
- [44] B. Chang, L.L. Li, D. Shi, et al., *Appl. Catal. B: Environ.* 283 (2021) 119622.
- [45] R.Q. Guo, J.L. Shi, K.W. Ma, et al., *J. Colloid Interface Sci.* 651 (2023) 172–181.
- [46] B.B. Fan, H.Z. Wang, H. Zhang, et al., *Adv. Funct. Mater.* 32 (2022) 2110783.
- [47] F.G. Wang, B. Li, Z.Y. Lin, et al., *Appl. Surf. Sci.* 592 (2022) 153245.